

## Research Article

# Plant-Mediated Synthesis of Ni-Doped CuO and Fe<sub>2</sub>O<sub>3</sub> Nanocomposite for Photodegradation of Methylene Blue Dye

Ermias Tafa Debele <sup>1</sup>, Temesgen Debelo Desissa,<sup>1</sup> Osman Ahmed Zelekew <sup>1</sup>,  
Fetene Fufa Bakare,<sup>1,2</sup> Gebisa Bekele Feyisa <sup>1</sup> and Tadele Hunde Wondimu <sup>1,2</sup>

<sup>1</sup>Department of Materials Science and Engineering, Adama Science and Technology University, P.O. Box 1888, Adama, Ethiopia

<sup>2</sup>Center of Excellence, Advanced Materials Science and Engineering, Adama Science and Technology University, Adama, Ethiopia

Correspondence should be addressed to Tadele Hunde Wondimu; tadechem@gmail.com

Received 21 November 2022; Revised 21 February 2023; Accepted 1 March 2023; Published 25 April 2023

Academic Editor: Van Viet Pham

Copyright © 2023 Ermias Tafa Debele et al. This is an open access article distributed under the Creative Commons Attribution License, which permits unrestricted use, distribution, and reproduction in any medium, provided the original work is properly cited.

Cu<sub>1-x</sub>Ni<sub>x</sub>O/Fe<sub>2</sub>O<sub>3</sub> (with  $x = 0.01, 0.02, 0.03, 0.04$  wt%) were synthesized by plant extraction technique. The absorbance and degradation performance of Ni-doped CuO and Fe<sub>2</sub>O<sub>3</sub> nanocomposite against methylene blue (MB) was analyzed, and the 2% Ni-doped CuO yielded an optimum result, and the optical bandgap of CuO, 2NCO, Fe<sub>2</sub>O<sub>3</sub>, and (60%) 2NCO/40% Fe<sub>2</sub>O<sub>3</sub> was found to be 1.88, 1.73, 2.1, and 1.80 eV, respectively. Hence, the 2% Ni-doped CuO (2NCO) was further used for the establishment of a composite with Fe<sub>2</sub>O<sub>3</sub>. The lowest composition of the oxide composite was (1-x) 2NCO/(x) Fe<sub>2</sub>O<sub>3</sub> ( $x = 0.1, 0.2, 0.3, 0.4, \text{ and } 0.5$ ). The degradation performance of those oxide composites was determined against (MB) with the nominal composition of sample (60%) 2NCO/40% Fe<sub>2</sub>O<sub>3</sub> resulted in an optimum degradation of MB with a percentage of 94% at 120 min. The recyclability takes a look at was performed for five cycles at the start of 94%; after five cycles, the sample remained stable at 120 min. Therefore, 2NCO/40% Fe<sub>2</sub>O<sub>3</sub> composite is going to be the selection material for waste product treatment.

## 1. Introduction

The need of eliminating organic contaminants and harmful heavy metal ions from water sources has increased in response to the rising demand for clean water [1]. MB is an organic contaminant that has devastating environmental effects due to its toxicity, carcinogenicity, mutagenicity, nonbiodegradability, and complex chemical structure. As a result, before they are released into the environment, these contaminants must be efficiently removed and/or converted to nontoxic molecules [2]. There are several techniques for removing and converting these contaminants have been developed. Some of these processes are flocculation [3], adsorption [4], biodegradation [4], sedimentation [5], and membrane process [6]. Since contaminants have complex chemical and physicochemical properties. Those techniques have limitations of low efficiency, high-energy consumption, and the risk of secondary pollutant formation are insufficient [7]. Furthermore, due to the presence of stable aromatic groups in the structure of organic pollutants, they are nondegradable using traditional techniques [8].

As a result, an alternative technique for removing and converting toxic molecules and substances from industrial effluents that is high in efficiency, low in energy consumption, and environmentally friendly is desired. One of the alternative approaches to treating industrial contaminants is photocatalysis, which uses photon energy and oxide semiconductor nanomaterials as a catalyst to degrade organic contaminants [9]. Metal oxides such as TiO<sub>2</sub> [10], ZnO [11], CeO<sub>2</sub> [12], CuO [13], Fe<sub>3</sub>O<sub>4</sub> [14], Fe<sub>2</sub>O<sub>3</sub> [15], BiVO<sub>4</sub> [16], and others have been studied for their photocatalytic activity due to the degradation of various organic pollutants. Catalysis by metal oxides under solar irradiation is primarily limited by a large bandgap, low charge transfer efficiency, and low recyclability. This limitation is improved by heterojunctions, metal or nonmetal doping. Green technology based on plants is becoming more popular as an eco-friendly, nontoxic, cost-effective, and safe option because plant extract-mediated biosynthesis of nanoparticles provides natural capping agents in the form of protein [17]. CuO and  $\alpha$ -Fe<sub>2</sub>O<sub>3</sub>, two important transition metal oxides, have been extensively studied and applied in a variety

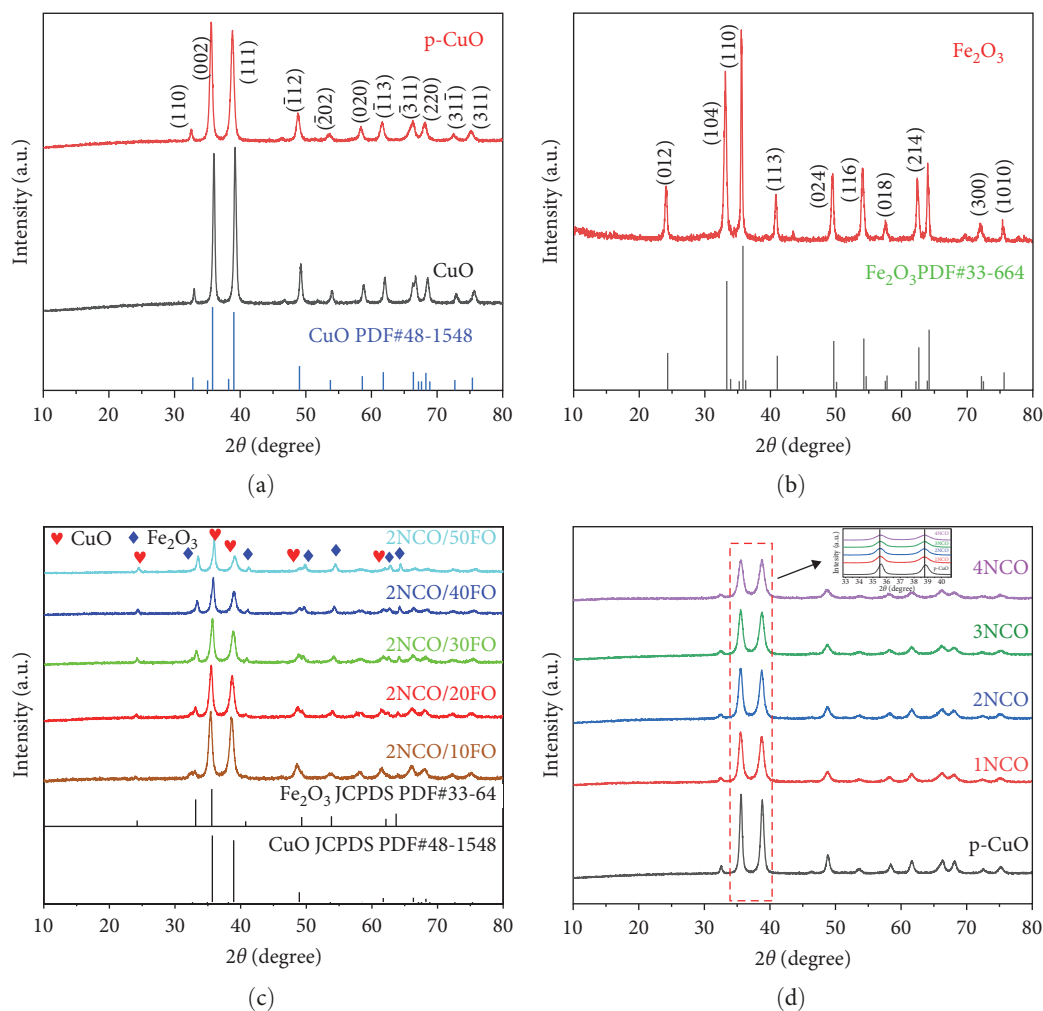


FIGURE 1: XRD result of (a) CuO, and p-CuO; (b)  $\text{Fe}_2\text{O}_3$ ; (c) p-CuO, 1NCO, 2NCO, 3NCO, and 4NCO; (d) CuO,  $\text{Fe}_2\text{O}_3$ , 2NCO/10FO, 2NCO/20FO, 2NCO/30FO, 2NCO/40FO, and 2NCO/50FO.

of fields, including catalysts [18], sensors [19], and electrochemistry [20]. Many methods have been used to create CuO/ $\text{Fe}_2\text{O}_3$  composites, including solid-phase reaction [21], hydrothermal [22], coprecipitation [23], sol-gel method [24]. The green synthesis method has advantages over other synthesis techniques due to its high yield, high product purity, no need for organic solvents, easy reproducibility, low cost, and environmentally friendly approach [25].

According to recent research, the photon property of CuO is important because of the variable oxidation states of copper, i.e.,  $\text{Cu}^+$ ,  $\text{Cu}^{2+}$ , and  $\text{Cu}^{3+}$ , which allows for both hole and electron doping [26]. Many changes have been reported as a result of transition metal doping into the CuO lattice, including Ni, Fe, Ti, Cd, and Zn doping [27]. To overcome metal oxide's limitations in photocatalytic applications. We designed a plant-mediated synthesis of Ni-doped CuO, and  $\text{Fe}_2\text{O}_3$  is found to be an interesting material for increasing the absorption of visible light. Hence, within the bandgap, transition metal ions can generate energy states. Furthermore, these act as stepping stones for electrons as they transition between the valence and conduction bands [26, 28].

In this work, plant-mediated Ni-doped CuO and  $\text{Fe}_2\text{O}_3$  composite have been used for the degradation of MB. Pristine CuO has low photocatalytic activity due to agglomeration and recombination problems. This problem was improved by doping with Ni with a similar ionic radius, forming a junction, and decreasing agglomeration by plant-mediated synthesis method of metal oxides. Moreover, there is no research has been conducted on photocatalyst material Ni-doped CuO and  $\text{Fe}_2\text{O}_3$  by plant-type *Acmella ciliata*, which was used as a capping/stabilizing agent during the synthesis of metal oxide for MB dye degradations.

## 2. Results and Discussion

**2.1. X-Ray Diffraction (XRD) Analysis.** The detailed synthesis experimental procedures of all catalysts were explained on pages s1 and s2 of Supplementary Material. Figure 1(a) XRD patterns of CuO and p-CuO confirming that the synthesized individual oxides with a single phase. The diffraction peaks at  $2\theta$  of  $32.51^\circ$ ,  $35.56^\circ$ ,  $38.92^\circ$ ,  $46.47^\circ$ ,  $48.84^\circ$ ,  $53.68^\circ$ ,  $58.4^\circ$ ,  $61.6^\circ$ ,  $66.3^\circ$ ,  $68.16^\circ$ ,  $72.46^\circ$ , and  $75.26^\circ$  were corresponded to (110), (002), (111), (-112), (-202), (020), (-113), (-311), (31-1), (220),

(311), and (004) crystallographic planes, respectively. In accordance with JCPDS card no: 48-1548, Figure 1(a) depicts a cubic crystal structure with a space group of  $C2/c$  [29]. The plant extracts CuO exhibits similar diffraction peaks and crystallographic planes. As shown in XRD patterns in Figure 1(b) of  $Fe_2O_3$ , the diffraction peaks at  $2\theta$  24.14°, 33.28°, 35.62°, 40.95°, 49.56°, 54.03°, 62.48°, 64.06°, 71.82°, 75.26°, and 77.26° corresponding to (012), (104), (110), (113), (024), (116), (018), (214), (300), (1010), and (220) planes, respectively. The  $Fe_2O_3$  contains a tetragonal crystal structure with space group  $R-3c$ ; the result observed was in close agreement with JCPD card no: 33-664 [30].

The XRD patterns of Figure 1(c) p-CuO, 1NCO, 2NCO, 3NCO, and 4NCO with their percentage compositions that show no other extra impurities exist for the doping concentration of Ni with 1, 2, 3, and 4 wt% as containing a cubic crystal structure. Because of the substitution of  $Ni^{2+}$  (0.69) with  $Cu^{2+}$  (0.73) sites in their monoclinic structure by similar ionic radii. Furthermore, the addition of Ni dopant to the CuO lattice had no effect on the lattice and only caused a minor shift in the  $2\theta$  values, as shown in the XRD inset in Figure 1(c). Different concentrations of nickel dopant list, which is 1%–4% are found in Table S1.

The XRD patterns, as shown in Figure 1(d), the main diffraction peaks are at  $2\theta$  of 35.5°, 38.7°, 48.7°, 58.3°, 61.6°, 66.2°, and 68.2° correspond to (-111), (111), (-202), (202), (-113), (-311), and (200) crystallographic planes, with the result closely matching the standard CuO JCPDS card no: 48-1548 [31]. The XRD pattern also presented intense diffraction peaks at  $2\theta$  of 24.1°, 33.1°, 40.9°, 49.4°, 54.0°, 62.4°, and 64.0° correspond to the (012), (104), (113), (024), (116), (214), and (300) crystallographic planes, respectively, and the result matched with standard  $Fe_2O_3$  JCPDS card no: 33-664 [32]. Nickel-doped copper oxide was prepared by adding 1 up to 4%, as shown in Table S1, and similar the synthesise procedure of composites was explained in percentage composition, also shown in Table S2.

The XRD patterns of Figure 1(c) p-CuO, 1NCO, 2NCO, 3NCO, and 4NCO show that there is no extra impurities exist for the doping concentration of Ni with 1, 2, 3, and 4 wt% containing a cubic crystal structure. Hence, the substitution of  $Ni^{2+}$  (0.69) with  $Cu^{2+}$  (0.73) sites in their monoclinic structure by similar ionic radii. Furthermore, the addition of Ni dopant to the CuO lattice had no effect on the lattice and only caused a minor shift in the  $2\theta$  values, as shown in the inset of Figure 1(c). The widening of XRD peak is due to the reduction in the crystallite size of CuO. Furthermore, there is no noticeable change in peak location, and the peaks are found to be fairly sharp and high intensity, implying that the produced powders have high crystallinity. The crystallite size was calculated using the Debye–Scherrer Equation (1) by measuring the full width at half maximum (FWHM) of the most intense diffraction peak [33].

$$D = \frac{k\lambda}{\beta \cos \theta}, \quad (1)$$

where  $\beta$  is the half-maximum intensity (FWHM) of the observed diffraction peak,  $k$  is the Scherrer constant 0.9

and  $\lambda$  is the X-ray wavelength (CuK radiation = 0.154 nm). The crystallinity of bare CuO, 1NCO, 2NCO, 3NCO, and 4NCO is 18.53, 9.51, 8.63, 7.76, and 7.67 nm, respectively. Additionally, 2NCO/10FO, 2NCO/30FO, 2NCO/40FO, and 2NCO/50FO were 13.12, 8.41, 8.85, 8.33, and 7.69 nm, respectively. The peak intensity decreases linearly as the FWHM increases with increasing Ni doping concentrations, indicating crystallinity degeneration of the CuO. The Ni ions move inside the CuO lattice and settle into the vacancy. The charge imbalance and ionic radius mismatch between Cu and Ni ions cause lattice distortion. CuO crystallization quality will be affected even more [34].

**2.2. Thermal Analysis.** Figure 2(a)–2(c) shows the thermogravimetric analysis (TGA)-DTA curves of composites 2NCO/10FO, 2NCO/30FO, and 2NCO/40FO. The first endothermic peak ( $\alpha$  region) for composites 2NCO/10FO, 2NCO/30FO, and 2NCO/40FO at a temperature around 75°C, with a weight loss of ~2%, 10.14%, and 10.6%, respectively, and this was due to the evaporation of residual water molecules adsorbed on the catalyst's surface [35, 36]. At a temperature around 300°C, the second step ( $\beta$  region) shows removal hydroxides with weight loss of around 6.76%, 19.73%, and 16.56% for 2NCO/10FO, 2NCO/30FO, and 2NCO/40FO, respectively. At a temperature of 300–550°C, a pronounced endothermic peak was observed in the third step ( $\gamma$  region), forming 2CNO/ $Fe_2O_3$ , respectively, and corresponding weight loss of ~7.81%, 19.52%, and 18.63%, respectively [37].

**2.3. Fourier Transform Infrared (FTIR) Analysis.** The functional groups and chemical structures of Acimella plant extract and powder CuO,  $Fe_2O_3$ , p-CuO, and 2NCO/40FO were discovered by analyzing the FTIR spectra, as shown in Figure 3. The broad peak centered at  $3,436\text{ cm}^{-1}$  corresponds to the stretching vibration of O–H, and there is a broadening of O–H covalent bond peaks, indicating that bond lengths of O–H covalent bonds have increased due to their involvement in hydrogen bonding [38]. The peak at  $875\text{ cm}^{-1}$  is due to C–H stretching vibration, and the strong band below  $700\text{ cm}^{-1}$  is assigned due to Fe–O stretching mode. The peaks at 647.626 and  $520\text{ cm}^{-1}$  correspond to the characteristic stretching vibrations of the Cu–O bond in monoclinic CuO NPs. The sample's characteristic absorption bands at  $555\text{ cm}^{-1}$  correspond to iron oxide stretching, while the bands around  $560\text{ cm}^{-1}$  correspond to the Fe–O stretching mode of the  $Fe_2O_3$  phase [39]. The other peaks observed in the spectra were caused by stabilizers and hydroxyls adsorbed on the surface of the oxide [40]. The Cu–O stretching mode was occurred due to the stretching along the (202) direction in CuO crystal peaks at around 439 and  $445\text{ cm}^{-1}$  [41].

**2.4. Morphological Analysis.** The morphology of CuO, p-CuO,  $Fe_2O_3$ , and 2NCO/40FO samples was examined using a scanning electron microscope (SEM). Figure 4(b) shows that the plant extract synthesized CuO shows well dispersed and decreased agglomeration, whereas CuO synthesized without plant extract is aggregated and not well dispersed. Figure 4(a) SEM image of CuO, (b) p-CuO, and (c)  $Fe_2O_3$ , and it was clearly observed that catalysts synthesized without plant extract are agglomerated together, and this may block access to catalyst

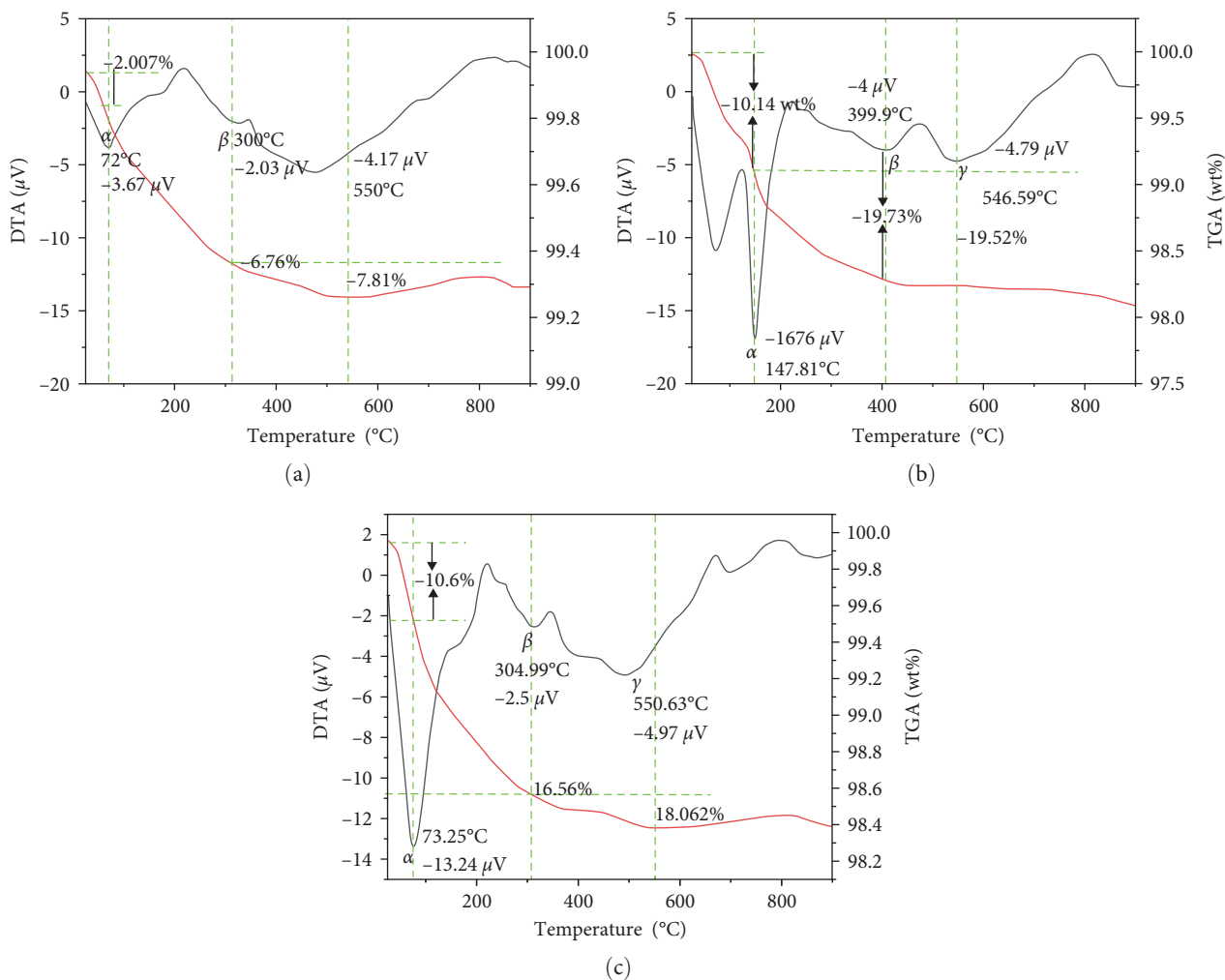


FIGURE 2: Thermogravimetric analysis of (a) 2NCO/10FO, (b) 2NCO/30FO, and (c) 2NCO/50FO.

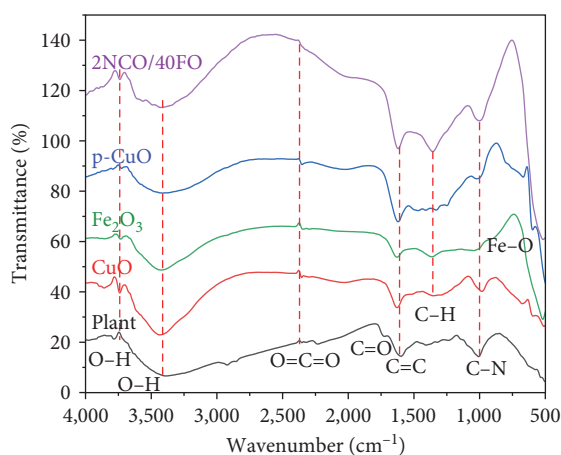


FIGURE 3: FTIR spectra of Acimella plant, CuO, Fe<sub>2</sub>O<sub>3</sub>, p-CuO, and 2NCO/40FO.

surfaces that result lower its performance toward the photocatalysis effect. Figure 4(d) shows that the composite 2NCO/40FO catalysts are well dispersed and particles small in size. The surface area and N<sub>2</sub> adsorption/desorption isotherm of

CuO, p-CuO, Fe<sub>2</sub>O<sub>3</sub>, and 2NCO/40FO show similar pore sizes, as explained in Table S3. The properties of being well dispersed, smaller particle in size, higher surface area, and higher pore volume provides access to the catalyst particle surfaces that may enhance its photocatalytic performance [37].

### 2.5. Ultraviolet-Visible (UV-Vis) and Optical Studies.

Figures 5(a) and 5(b) show that the optical absorption spectra of the samples CuO, Fe<sub>2</sub>O<sub>3</sub>, 1NCO, 2NCO, 3NCO, 4NCO, 2NCO/10FO, 2NCO/20FO, 2NCO/30FO, and 2NCO/40FO, 2NCO/50FO exhibit band edge absorption peak at 367.44 nm, whereas Figure 6(a)–6(d) show that the optical bandgap values estimation of samples Fe<sub>2</sub>O<sub>3</sub>, CuO, 2NCO, and 2NCO/40FO is 2.1, 1.88, 1.73, and 1.80 eV, respectively, which is calculated using the Tauc relation Equation (2).

$$(\alpha h\nu)^2 = A(h\nu - E_g). \quad (2)$$

$E_g$  stands for optical bandgap energy,  $\nu$  for frequency,  $h$  for Planck's constant, and  $A$  for a transition probability constant [42]. The bandgap value clearly indicates that 2NCO/40FO reduces the bandgap energy. The catalyst absorbs more light as the bandgap narrows, allowing electrons to readily

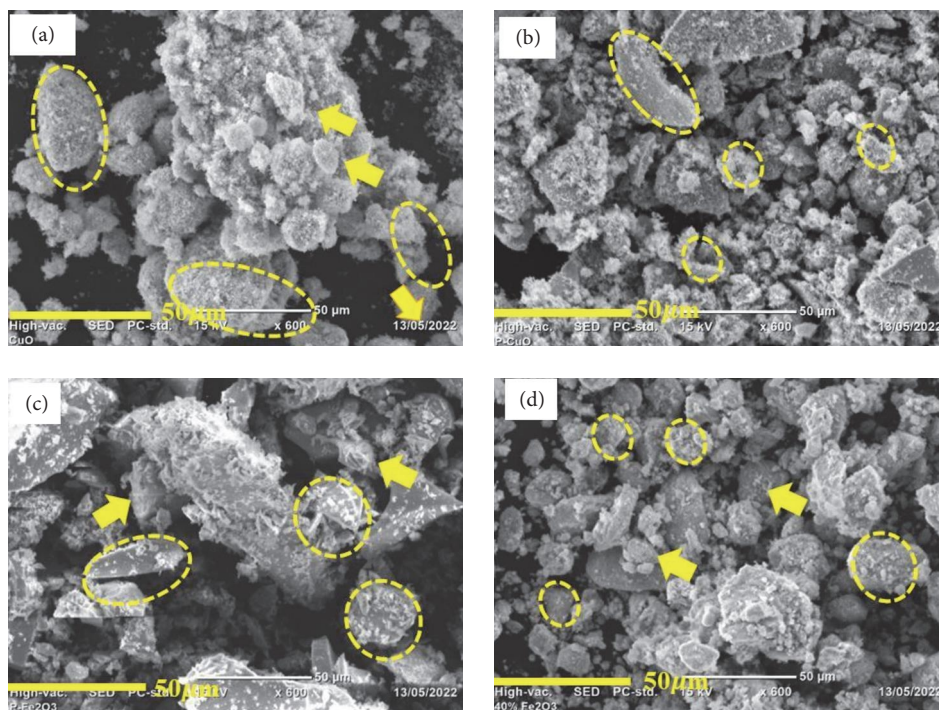


FIGURE 4: SEM morphological analysis of (a) CuO, (b) p-CuO, (c) Fe<sub>2</sub>O<sub>3</sub>, and (d) 2NCO/40FO.

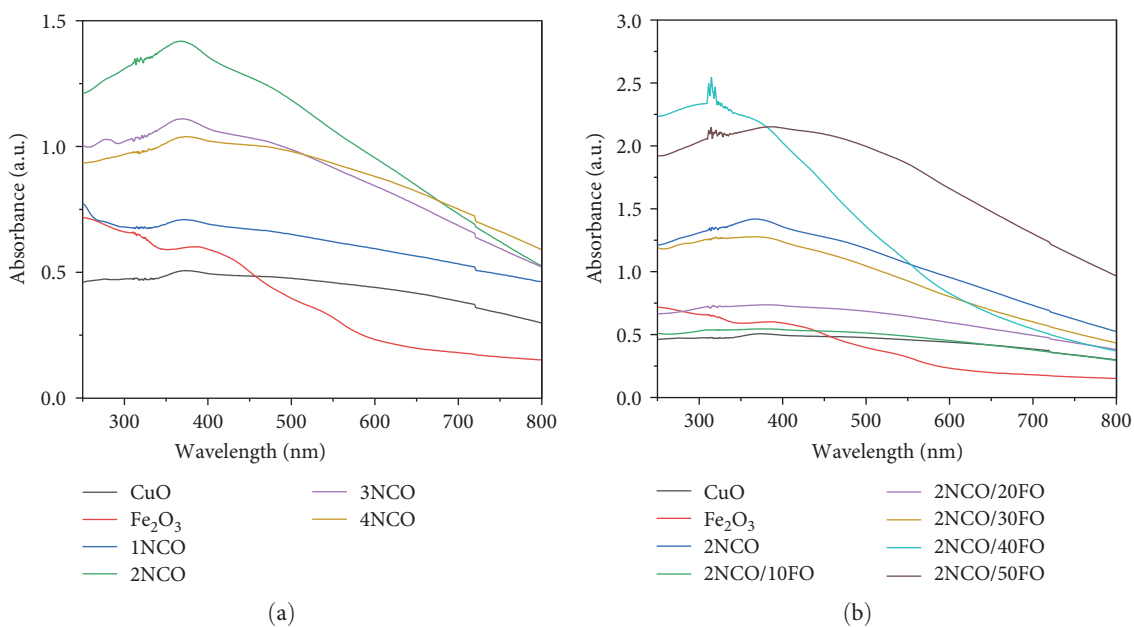


FIGURE 5: Absorbance spectra of (a) CuO, Fe<sub>2</sub>O<sub>3</sub>, 1NCO, 2NCO, 3NCO, 4NCO; (b) CuO, Fe<sub>2</sub>O<sub>3</sub>, 2NCO/10FO, 2NCO/20FO, 2NCO/30FO, 2NCO/40FO, and 2NCO/50FO.

jump from the valance to the conduction band, and the formation of electron and hole pairs is essential in the dye degradation process.

**2.6. Photoluminescence (PL) Analysis.** PL is used to study the separation of photogenerated charge carriers because the PL signal is generally caused by the recombination of photogenerated electron–hole pairs. From the comparative PL spectra

presented in Figure 7 of synthesized CuO, 2NCO, Fe<sub>2</sub>O<sub>3</sub>, and 2NCO/40FO. The PL-exhibited emission peaks in the 424.94 nm region under an excitation wavelength of 270 nm [43]. The PL intensity of Fe<sub>2</sub>O<sub>3</sub> and 2NCO was found to be lower than that of pure CuO, indicating that Fe<sub>2</sub>O<sub>3</sub> and 2NCO had greater charge separation than bare CuO due to bandgap and surface defects or interstitial defects. Therefore, the decrease in PL intensity of 2NCO/40FO may imply a low

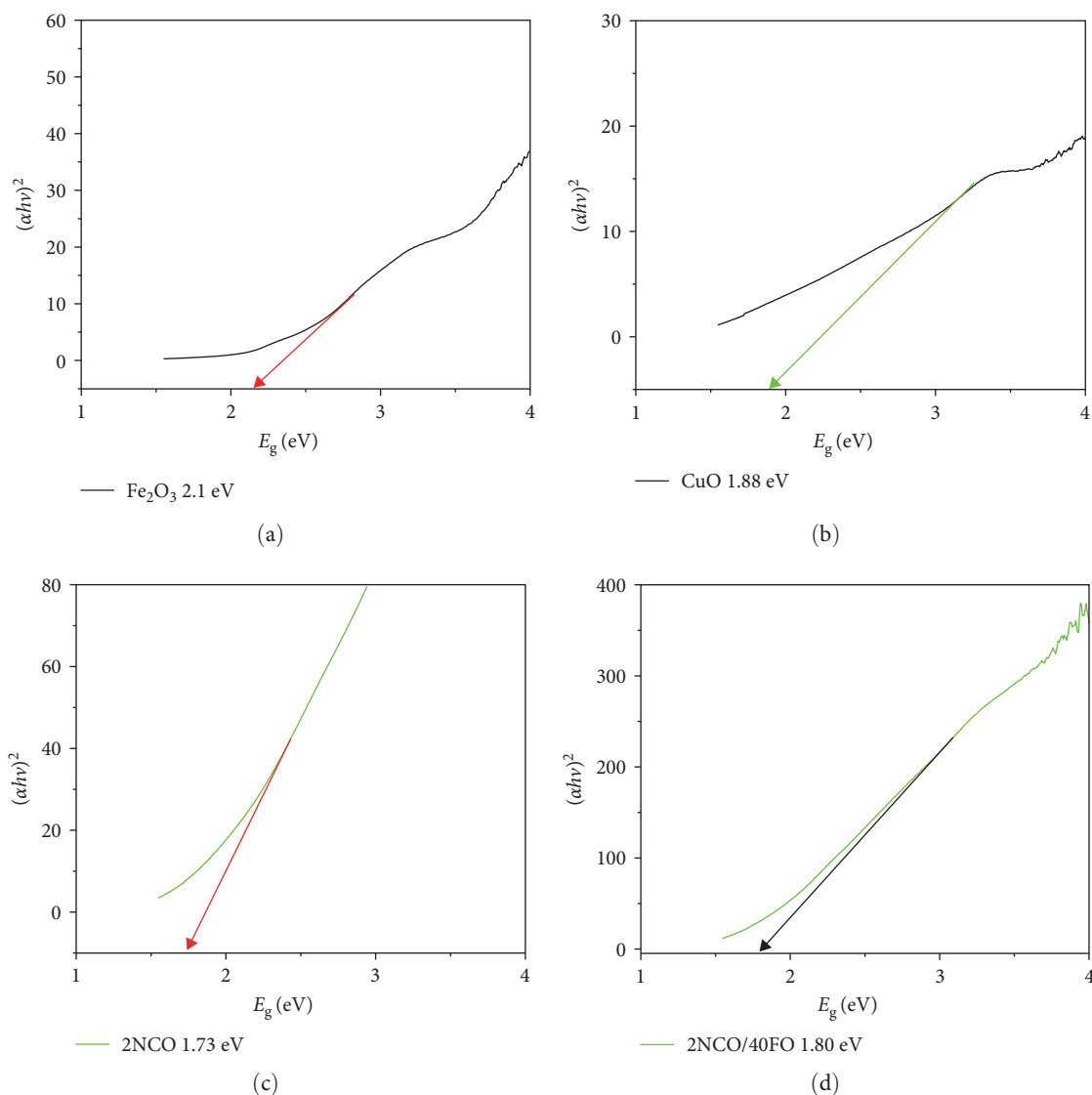


FIGURE 6: Tauc plot optical bandgap estimation (a)  $\text{Fe}_2\text{O}_3$ , (b)  $\text{CuO}$ , (c) 2NCO, and (d) 2NCO/40FO.

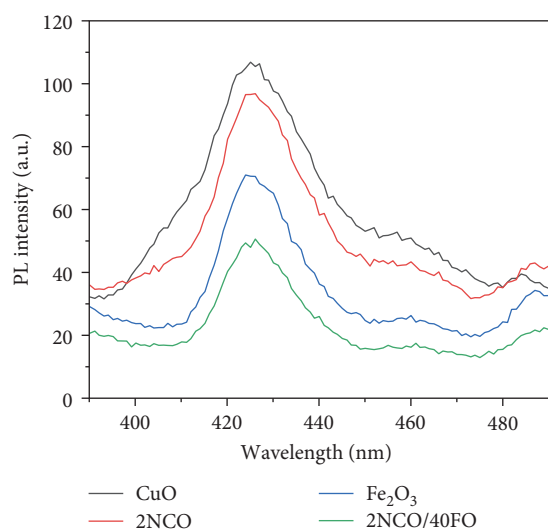


FIGURE 7: PL spectra of synthesized  $\text{CuO}$ , 2NCO,  $\text{Fe}_2\text{O}_3$ , and 2NCO/40FO.

$e^-/h^+$  pair recombination rate and high photon efficiency of the catalyst, explaining the rise in photocatalytic activity [44].

### 2.7. Electrochemical Impedance Spectroscopy (EIS) Studies.

This EIS result was measured in 0.1 M  $\text{Na}_2\text{SO}_4$ , frequency of 0.1 Hz–100 kHz, and 10 mV applied potential versus  $\text{Ag}/\text{AgCl}/\text{Cl}^-$  reference electrode to check the conductivity properties of the catalysts. The EIS Nyquist plot's arc radius indicates that the interface layer resistance occurs at the electrode's surface. Figure 8 shows that the arc radius decreases for samples 2NCO,  $\text{Fe}_2\text{O}_3$ , and 2NCO/40FO than  $\text{CuO}$  due to the increased dipole moment; 2NCO/40FO has a lower arc radius than the other. During photocatalytic reaction tests, the composite 2NCO/40FO allows for faster charge separation and transfer of photogenerated charge carriers. The PL result in Figure 7 confirms that composite 2NCO/40FO has better charge separation. Hence, the obtained composite lowers the photogenerated electron–hole pair recombination,

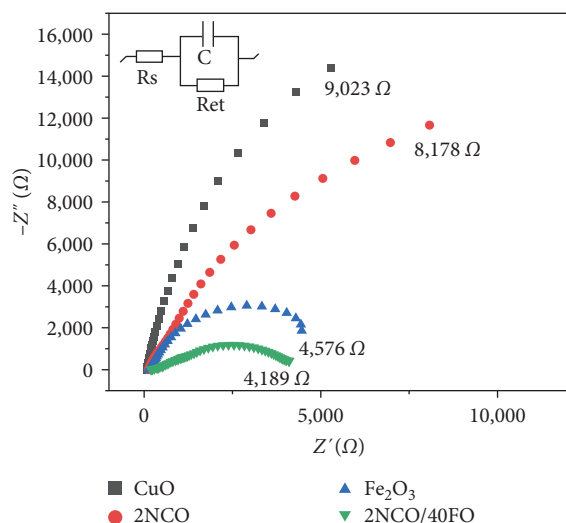


FIGURE 8: EIS of CuO, 2NCO, Fe<sub>2</sub>O<sub>3</sub>, 2NCO/40FO.

which results high photocatalytic activity toward dye degradation [45–47].

**2.8. Photocatalytic Dye Degradation.** The UV–Vis spectroscopy was used to examine the degradation percentage ( $D\%$ ), which is calculated by using Equation (3).

$$D\% = \frac{C_0 - C_t}{C_0} \times 100\%, \quad (3)$$

where  $C_0$  and  $C_t$  are the dye concentrations at 0 and  $t$  minutes of irradiation, respectively. The absorbance versus wavelength plot was calculated using the Beer–Lambert rule using equation S4 and UV–Vis absorption spectra of MB solution at different light exposure time durations. The degradation efficiency, as shown in Figure 9 calculated using Equation (3) and for (a) CuO (68%), (b) p-CuO (74%), (c) 2NCO (81%), (d) Fe<sub>2</sub>O<sub>3</sub> (84%), (e) 2NCO/40FO (94%). Figure S1 shows the degradation efficiency of (a) 1NCO (76%), (b) 3NCO (78%), (c) 4NCO (77%). The degradation efficiency of (a) 2NCO/10FO (81%), (b) 2NCO/20FO (84%), (c) 2NCO/30FO (86%), and (d) 2NCO/50FO (90%) at 120 min and UV–Vis absorption spectra of MB solution at different light exposure time durations of (a) 1NCO, (b) 3NCO, and (c) 4NCO, as shown in Figures S1 and S2. The photocatalyst efficiency of CuO was lower than CuO synthesized with plant extract. The plant-extracted CuO improved the surface area and charge carriers for MB dye degradation [48]. On the other hand, doping increases the photocatalytic activity of the catalyst by concentrating the target molecules (organic pollutants) at the catalyst surface by forming a Lewis acid–base combination, and as the doping concentration is increased, the degradation efficiency increased up to 2% Ni and then decreased and the optimum level of Ni-dopant is 2%. The use of Ni-dopant at the donor level avoids the recombination of excited electrons and holes in the valance band within the semiconductor. The crystalline size calculated from XRD result by Sherer’s Equation (1) and the 2NCO shows that optimum

crystallinity due to its comparable effect. The crystalline size should be neither large nor too small; it should be optimum and comparable with its surface area. Figure 5(a) shows that the absorbance of 2NCO has high absorption property. Hence, the catalyst easily absorbs light and makes electrons travel from the valance band to the conduction band more than the others [49]. The composite of 2NCO/40FO was more efficient than the others due to the existence of secondary metabolites present in plant extract and metal ions present in the composite.

**2.9. Kinetics Study.** The photodegradation rates of MB were faster with 2NCO/40FO composite than bare CuO under the same conditions, as shown in Figure 10(a). The pseudo 1st order model was used to study the kinetic degradation of MB dye photodegradation at neutral pH utilizing CuO, p-CuO, Fe<sub>2</sub>O<sub>3</sub>, 2NCO, and 2NCO/40FO composite using Equation (4).

$$-\ln \frac{C_t}{C_0} = KT, \quad (4)$$

where  $C_t$  is the MB concentration at irradiation time  $t$ ,  $C_0$  is the preirradiation concentration,  $K$  is the first order rate constant ( $\text{min}^{-1}$ ), and  $T$  is the temprature [50]. Then plotting  $\ln (C_t/C_0)$  vs.  $t$  as shown in Figure 10(b) and the value of reaction rate was exhibited in Figure 10(c) was calculated for CuO, p-CuO, 2NCO, Fe<sub>2</sub>O<sub>3</sub>, and 2NCO/40FO, to be 0.00969, 0.01147, 0.01322, 0.01498, 0.02301, 0.77079, 0.84899, 1.619 1.57458, and 3.35464  $\text{min}^{-1}$ , respectively. 2NCO/40FO shows a higher kinetic rate than pure CuO, and the introduction of Fe<sub>2</sub>O<sub>3</sub> in 2NCO can further increase to some extent. The data fitted well and gave a correlation coefficient of CuO, p-CuO, 2NCO, Fe<sub>2</sub>O<sub>3</sub>, and 2NCO/40FO, 0.93705, 0.93844, 0.94696, 0.94711, and 0.95389 at the neutral pH, respectively.

**2.10. Stability and Recyclability.** For pilot-scale remediation systems, recovery and reusability of the photocatalyst are important parameters to be considered. Figure 11 depicts the recyclability and stability of the 2NCO/40FO catalyst after five cycles for 120 min reaction, and it is 0.125 g catalyst in 500 ml of the MB dye. This clearly indicated that the catalyst was recycled and reused after MB dye degradation. In the high-efficiency cycles, the performance of 2NCO/40FO attended from 94% to 80% after five cycles. There is a material loss during the recovery process (washing and drying), leading to a reduced dose in succeeding cycles, lowering surface catalytic activity and lowering performance [51]. The recyclability and stability test showed the catalyst was stable for up to five cycles. The XRD results of reused catalyst showed the reused material showed no change in crystal structure in the XRD pattern. In keeping with the findings, current materials systems degrade an organic MB dye from industrial effluents created by numerous processes. Therefore, the 2NCO/40FO photocatalyst was no significant change up to five cycles successfully for degrading of MB dye under visible light irradiation.

**2.11. The Proposed Dye Degradation Mechanism of 2NCO/40FO Nanocomposite.** The photocatalytic mechanism of CuO/Fe<sub>2</sub>O<sub>3</sub> composites is depicted in Figure 12. During UV

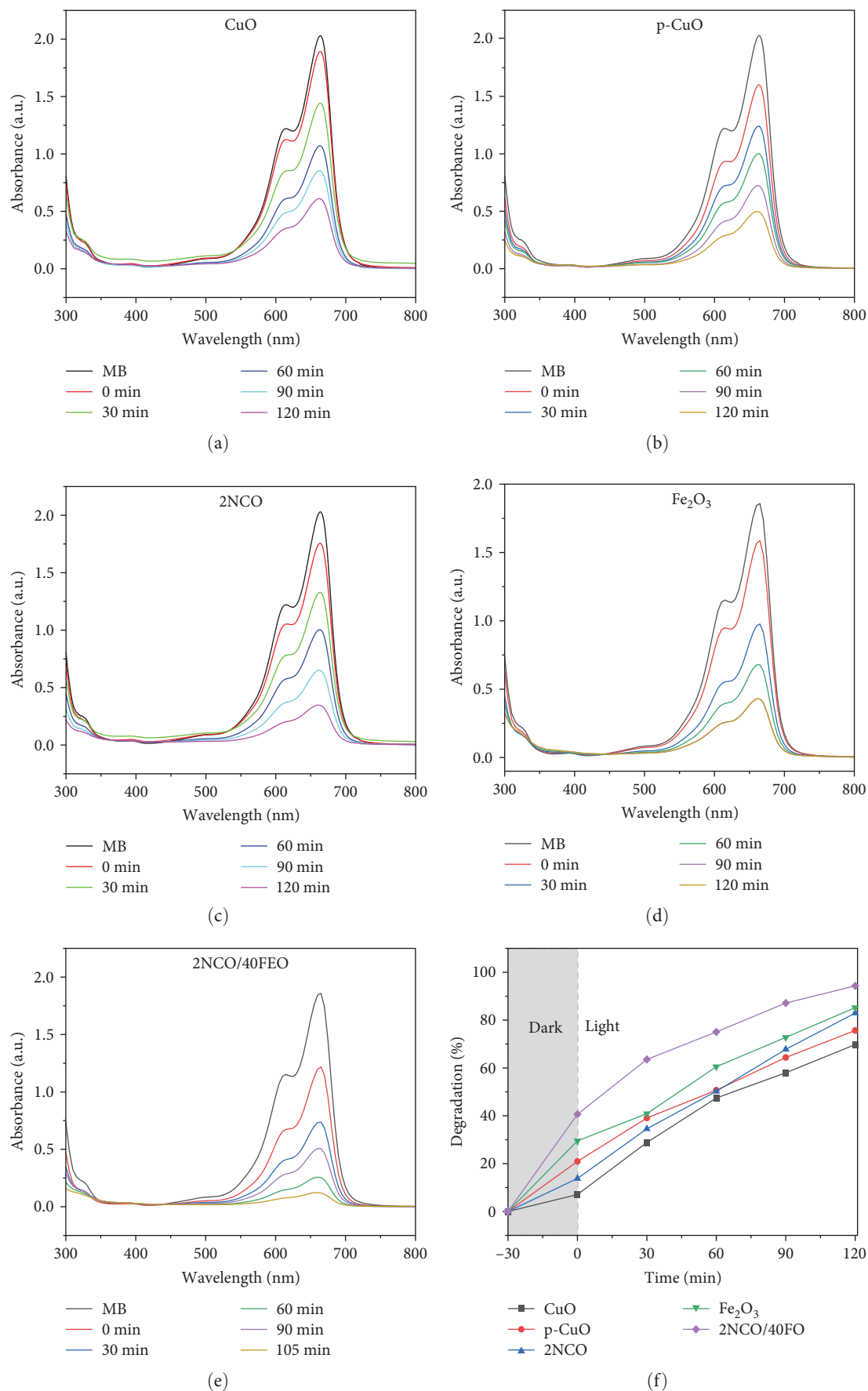


FIGURE 9: UV-Vis absorption spectra of MB solution at different light exposure time durations of (a) CuO, (b) p-CuO, (c) Fe<sub>2</sub>O<sub>3</sub>, (d) 2NCO, and (e) 2NCO/40FO; the degradation performance of MB, (f) CuO, p-CuO, Fe<sub>2</sub>O<sub>3</sub>, and 2NCO/40FO.

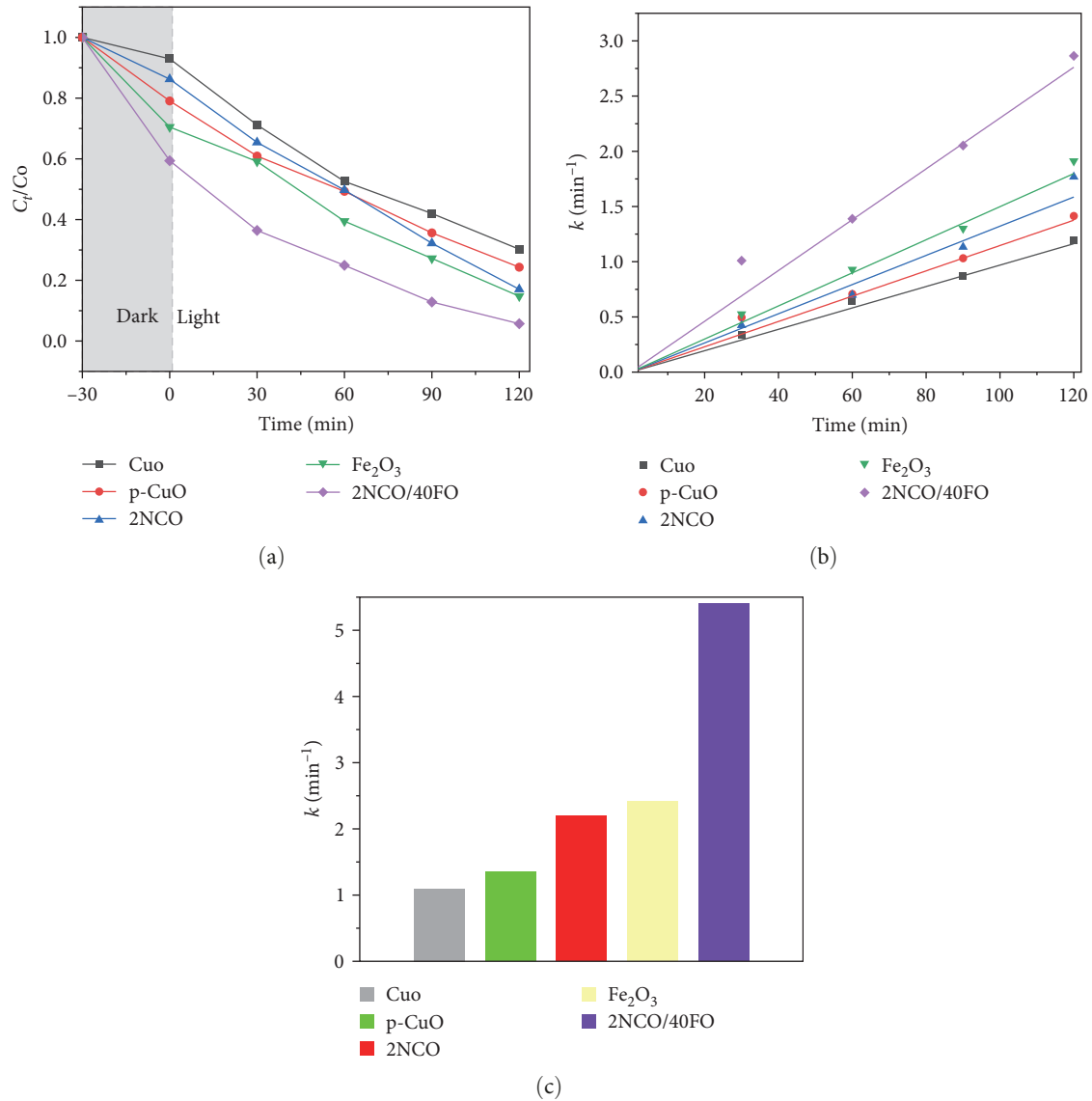
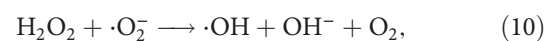
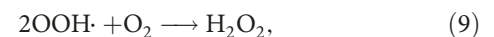
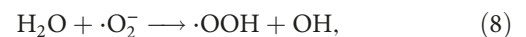
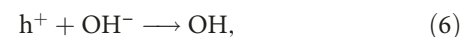
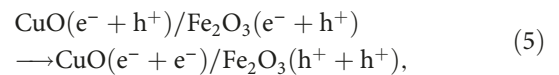


FIGURE 10: (a) The variation of MB concentration under visible irradiation at different periods, (b) the consistent reaction kinetics of photodegradation of MB, (c) the reaction rate constant of CuO, p-CuO, 2NCO, Fe<sub>2</sub>O<sub>3</sub>, and 2NCO/40FO catalysts.

light irradiation, electrons from the CuO and Fe<sub>2</sub>O<sub>3</sub> valence bands (VB) are promoted to the conduction band (CB), leaving holes in the VB ( $h^+ \text{ VB}$ ). The heterostructure creates a good couple, which helps separate the created electron-hole pairs [52]. CuO was doped with (2%) Ni to improve its electron transport properties. The difference in conduction band levels, electrons stored in the CuO conduction band travel to the Fe<sub>2</sub>O<sub>3</sub> conduction band. Furthermore, the reaction between absorbed oxygen ( $O_2$ ) and electrons collected at the surface of Fe<sub>2</sub>O<sub>3</sub> results in the formation of superoxide radical ( $\cdot O_2^-$ ) as electrons in Fe<sub>2</sub>O<sub>3</sub> conduction band reduce absorbed  $O_2$ . The MB dye was degraded by the superoxide radical and electrons that were generated [53]. However, the valence band holes in CuO and Fe<sub>2</sub>O<sub>3</sub> barely met the criteria for the generation of hydroxyl radicals ( $\cdot OH$ ) ( $H_2O/\cdot OH^-$ ) instead ( $\cdot OH$ ) formed from the intermediate reaction shown in the following equations. The holes and hydroxyl radicals may play a role in

the degradation process, as shown in the equations below. Finally, the process produced intermediate molecules such as  $H_2O$  and  $CO_2$ .



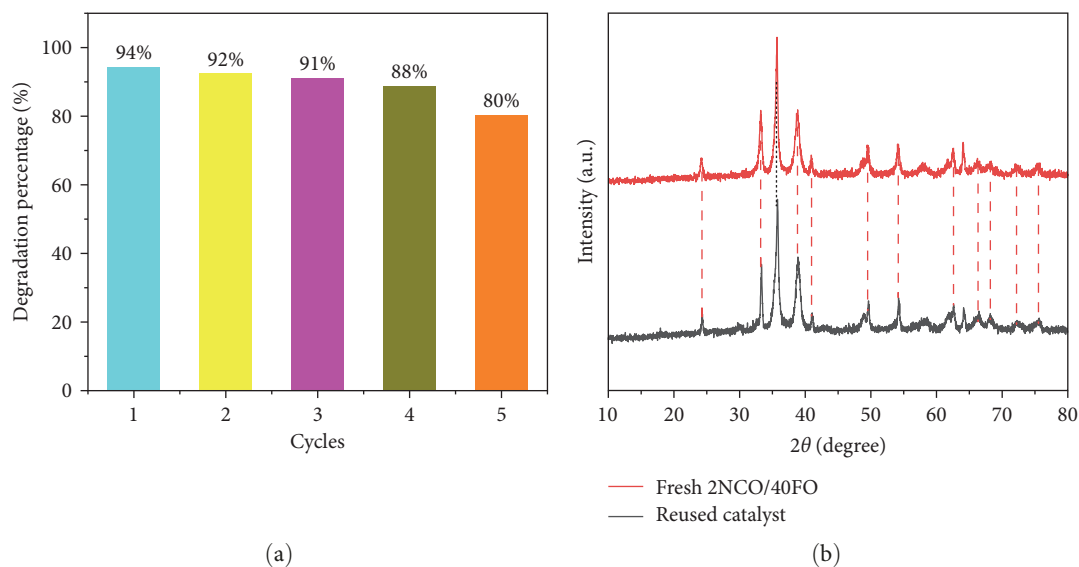


FIGURE 11: (a) Bar graph of stability and Recyclability, (b) XRD pattern of fresh 2NCO/40FO and reused catalyst.

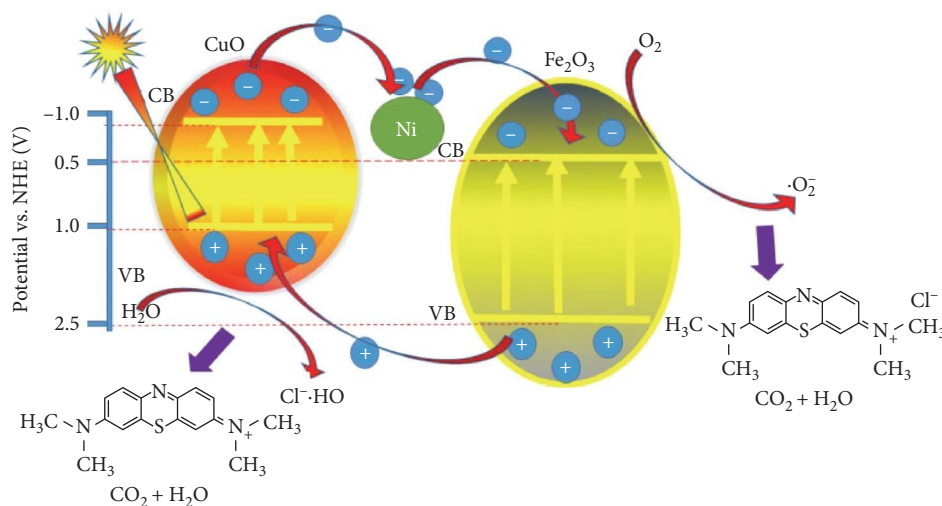
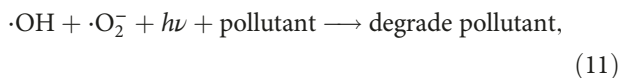


FIGURE 12: Mechanism of photodegradation of 2NCO/40FO.



### 3. Conclusion

In the present work, CuO, p-CuO, Fe<sub>2</sub>O<sub>3</sub>, 1NCO, 2NCO, 3NCO, 4NCO, 2NCO/10FO, 2NCO/20FO, 2NCO/30FO, 2NCO/40FO, and 2NCO/50FO catalyst were successfully synthesized by plant-mediated extract, which is green

synthesis method. The prepared materials were characterized by XRD, TGA, FTIR, PL, and EIS. The 2NCO/40FO catalyst shows lowered recombination and better charge transfer resistance. The performance of bare CuO was 68%, while the plant-extracted green synthesized CuO shows better degradation performance, and the synthesized Fe<sub>2</sub>O<sub>3</sub> showed a degradation percentage of 81% and optimization of Ni-doped copper oxide with a doping concentration of 2% Ni-doped CuO was 80% maximum absorbance properties. The boosted photocatalytic property was assessed by coupling 2NCO coupled with Fe<sub>2</sub>O<sub>3</sub> with weight percentages of 40% Fe<sub>2</sub>O<sub>3</sub> with 2NCO/40FO was shown 94% and better absorbance properties. The recyclability and stability test showed the catalyst was stable up to five cycles, and the XRD result of

reused catalyst showed no change in the XRD pattern. Consequently, the material will degrade organic MB dye, which is from different textile industrials effluents.

### Data Availability

The finding of this study is supported by supplementary data and main manuscript (article).

### Conflicts of Interest

The authors declare that they have no conflicts of interest.

### Acknowledgments

We acknowledge the Adama Science and Technology University for funding and materials support.

### Supplementary Materials

The experimental part. (*Supplementary Materials*)

### References

- [1] M. Salehi, "Global water shortage and potable water safety; today's concern and tomorrow's crisis," *Environment International*, vol. 158, Article ID 106936, 2022.
- [2] A. M. Abbas, M. Abid, K. N. Abbas, W. J. Aziz, and A. Salim, "Photocatalytic activity of Ag-ZnO nanocomposites integrated essential ginger oil fabricated by green synthesis method," *Journal of Physics: Conference Series*, vol. 1892, Article ID 012005, 2021.
- [3] Z. Yang, M. Li, M. Yu et al., "A novel approach for methylene blue removal by calcium dodecyl sulfate enhanced precipitation and microbial flocculant GA1 flocculation," *Chemical Engineering Journal*, vol. 303, pp. 1–13, 2016.
- [4] M. Dauda, *Adsorption of Cadmium and Phenol on Sludge based Activated Carbon*, King Fahd University of Petroleum and Minerals, Saudi Arabia, 2016.
- [5] W. Zhang, C. Huo, B. Hou et al., "Secondary particle size determining sedimentation and adsorption kinetics of titanate-based materials for ammonia nitrogen and methylene blue removal," *Journal of Molecular Liquids*, vol. 343, Article ID 117026, 2021.
- [6] N. Nasrollahi, V. Vatanpour, and A. Khataee, "Removal of antibiotics from wastewaters by membrane technology: limitations, successes, and future improvements," *Science of the Total Environment*, vol. 838, Part 1, Article ID 156010, 2022.
- [7] O. M. Rodriguez-Narvaez, J. M. Peralta-Hernandez, A. Goonetilleke, and E. R. Bandala, "Treatment technologies for emerging contaminants in water: a review," *Chemical Engineering Journal*, vol. 323, pp. 361–380, 2017.
- [8] S. Jalali, M. R. Rahimi, K. Dashtian, M. Ghaedi, and S. Mosleh, "One step integration of plasmonic Ag<sub>2</sub>CrO<sub>4</sub>/Ag/AgCl into HKUST-1-MOF as novel visible-light driven photocatalyst for highly efficient degradation of mixture dyes pollutants: its photocatalytic mechanism and modeling," *Polyhedron*, vol. 166, pp. 217–225, 2019.
- [9] C. Sivaraman, S. Vijayalakshmi, E. Leonard, S. Sagadevan, and R. Jambulingam, "Current developments in the effective removal of environmental pollutants through photocatalytic degradation using nanomaterials," *Catalysts*, vol. 12, no. 5, Article ID 544, 2022.
- [10] S. Lakshmi, R. Renganathan, and S. Fujita, "Study on TiO<sub>2</sub>-mediated photocatalytic degradation of methylene blue," *Journal of Photochemistry and Photobiology A: Chemistry*, vol. 88, no. 2-3, pp. 163–167, 1995.
- [11] W. S. Chiu, P. S. Khiew, M. Cloke et al., "Photocatalytic study of two-dimensional ZnO nanopellets in the decomposition of methylene blue," *Chemical Engineering Journal*, vol. 158, no. 2, pp. 345–352, 2010.
- [12] H. Pouretedal and A. Kadkhodaie, "Synthetic CeO<sub>2</sub> nanoparticle catalysis of methylene blue photodegradation: kinetics and mechanism," *Chinese Journal of Catalysis*, vol. 31, no. 11-12, pp. 1328–1334, 2010.
- [13] A. G. Acedo-Mendoza, A. Infantes-Molina, D. Vargas-Hernández, C. A. Chávez-Sánchez, E. Rodríguez-Castellón, and J. C. Tánori-Córdova, "Photodegradation of methylene blue and methyl orange with CuO supported on ZnO photocatalysts: the effect of copper loading and reaction temperature," *Materials Science in Semiconductor Processing*, vol. 119, Article ID 105257, 2020.
- [14] D. Uzunoğlu, M. Ergüt, P. Karacabey, and A. Özer, "Synthesis of cobalt ferrite nanoparticles via chemical precipitation as an effective photocatalyst for photo Fenton-like degradation of methylene blue," *Desalination and Water Treatment*, vol. 172, pp. 96–105, 2019.
- [15] E. A. Abdelrahman, R. M. Hegazey, Y. H. Kotp, and A. Alharbi, "Facile synthesis of Fe<sub>2</sub>O<sub>3</sub> nanoparticles from Egyptian insecticide cans for efficient photocatalytic degradation of methylene blue and crystal violet dyes," *Spectrochimica Acta Part A: Molecular and Biomolecular Spectroscopy*, vol. 222, Article ID 117195, 2019.
- [16] B. Zhou, X. Zhao, H. Liu, J. Qu, and C. P. Huang, "Visible-light sensitive cobalt-doped BiVO<sub>4</sub> (Co-BiVO<sub>4</sub>) photocatalytic composites for the degradation of methylene blue dye in dilute aqueous solutions," *Applied Catalysis B: Environmental*, vol. 99, no. 1-2, pp. 214–221, 2010.
- [17] M. H. Kahsay, A. Tadesse, D. RamaDevi, N. Belachew, and K. Basavaiah, "Green synthesis of zinc oxide nanostructures and investigation of their photocatalytic and bactericidal applications," *RSC Advances*, vol. 9, no. 63, pp. 36967–36981, 2019.
- [18] H. Liu, Y. Wei, P. Li, Y. Zhang, and Y. Sun, "Catalytic synthesis of nanosized hematite particles in solution," *Materials Chemistry and Physics*, vol. 102, no. 1, pp. 1–6, 2007.
- [19] K. Song, Q. Wang, Q. Liu, H. Zhang, and Y. Cheng, "A wireless electronic nose system using a Fe<sub>2</sub>O<sub>3</sub> gas sensing array and least squares support vector regression," *Sensors*, vol. 11, pp. 485–505, 2011.
- [20] M. Bomio, P. Lavela, and J. L. Tirado, "Electrochemical evaluation of CuFe<sub>2</sub>O<sub>4</sub> samples obtained by sol-gel methods used as anodes in lithium batteries," *Journal of Solid State Electrochemistry*, vol. 12, pp. 729–737, 2008.
- [21] Y. Wang, X. Xia, J. Zhu, Y. Li, X. Wang, and X. Hu, "Catalytic activity of nanometer-sized CuO/Fe<sub>2</sub>O<sub>3</sub> on thermal decomposition of AP and combustion of AP-based propellant," *Combustion Science and Technology*, vol. 183, no. 2, pp. 154–162, 2010.
- [22] X.-M. Liu, W.-D. Yin, S.-B. Miao, and B.-M. Ji, "Fabrication of CuO/Fe<sub>2</sub>O<sub>3</sub> hollow hybrid microspheres," *Materials Chemistry and Physics*, vol. 113, no. 2-3, pp. 518–522, 2009.
- [23] Y. Li and Y.-L. Wu, "An over four millennium story behind qinghaosu (Artemisinin)—a fantastic antimalarial drug from a traditional Chinese herb," *Current Medicinal Chemistry*, vol. 10, no. 21, pp. 2197–2230, 2003.
- [24] X. Ma, X. Feng, X. He, H. Guo, and L. Lü, "Preparation, characterization and catalytic behavior of hierarchically porous CuO/ $\alpha$ -Fe<sub>2</sub>O<sub>3</sub>/SiO<sub>2</sub> composite material for CO and *o*-DCB

- oxidation," *Journal of Natural Gas Chemistry*, vol. 20, no. 6, pp. 618–622, 2011.
- [25] G. B. Nair, V. B. Pawade, and S. J. Dhoble, "White light-emitting novel nanophosphors for LED applications," in *Nanomaterials for Green Energy*, B. A. Bhanvase, V. B. Pawade, S. J. Dhoble, S. H. Sonawane, and M. Ashokkumar, Eds., pp. 411–431, Elsevier, 2018.
- [26] W. Gao, S. Yang, S. Yang, L. Lv, and Y. Du, "Synthesis and magnetic properties of Mn doped CuO nanowires," *Physics Letters A*, vol. 375, no. 2, pp. 180–182, 2010.
- [27] C. T. Meneses, J. G. S. Duque, L. G. Vivas, and M. Knobel, "Synthesis and characterization of TM-doped CuO (TM = Fe, Ni)," *Journal of Non-Crystalline Solids*, vol. 354, no. 42–44, pp. 4830–4832, 2008.
- [28] Y. Gülen, F. Bayansal, B. Şahin, H. A. Çetinkara, and H. S. Güder, "Fabrication and characterization of Mn-doped CuO thin films by the SILAR method," *Ceramics International*, vol. 39, no. 6, pp. 6475–6480, 2013.
- [29] P. Raizada, A. Sudhaik, S. Patial et al., "Engineering nanostructures of CuO-based photocatalysts for water treatment: current progress and future challenges," *Arabian Journal of Chemistry*, vol. 13, no. 11, pp. 8424–8457, 2020.
- [30] M. Mahadik, S. Shinde, V. Mohite et al., "Photoelectrocatalytic oxidation of Rhodamine B with sprayed  $\alpha$ -Fe<sub>2</sub>O<sub>3</sub> photocatalyst," *Materials Express*, vol. 3, no. 3, pp. 247–255, 2013.
- [31] S. Nazarath Begum, A. Esakkiraja, and S. Mohamed Asan, "Green synthesis, characterization and antibacterial activity of copper oxide nanoparticles synthesized using catharanthus roseus leaf extract," *Journal of Applied Science and Computations*, vol. 6, no. 6, pp. 3228–3240, 2019.
- [32] M. Sun, Y. Lei, H. Cheng et al., "Mg doped CuO–Fe<sub>2</sub>O<sub>3</sub> composites activated by persulfate as highly active heterogeneous catalysts for the degradation of organic pollutants," *Journal of Alloys and Compounds*, vol. 825, Article ID 154036, 2020.
- [33] C. Ramamoorthy and V. Rajendran, "Synthesis and characterization of CuS nanostructures: structural, optical, electrochemical and photocatalytic activity by the hydro/solvothermal process," *International Journal of Hydrogen Energy*, vol. 42, no. 42, pp. 26454–26463, 2017.
- [34] L. V. Devi, T. Selvalakshmi, S. Sellaiyan, A. Uedono, K. Sivaji, and S. Sankar, "Effect of La doping on the lattice defects and photoluminescence properties of CuO," *Journal of Alloys and Compounds*, vol. 709, pp. 496–504, 2017.
- [35] X. Zhou, T. Su, Y. Jiang, Z. Qin, H. Ji, and Z. Guo, "CuO–Fe<sub>2</sub>O<sub>3</sub>–CeO<sub>2</sub>/HZSM-5 bifunctional catalyst hydrogenated CO<sub>2</sub> for enhanced dimethyl ether synthesis," *Chemical Engineering Science*, vol. 153, pp. 10–20, 2016.
- [36] R.-W. Liu, Z.-Z. Qin, H.-B. Ji, and T.-M. Su, "Synthesis of dimethyl ether from CO<sub>2</sub> and H<sub>2</sub> using a Cu–Fe–Zr/HZSM-5 catalyst system," *Industrial & Engineering Chemistry Research*, vol. 52, no. 47, pp. 16648–16655, 2013.
- [37] G. Bonura, M. Cordaro, C. Cannilla et al., "Catalytic behaviour of a bifunctional system for the one step synthesis of DME by CO<sub>2</sub> hydrogenation," *Catalysis Today*, vol. 228, pp. 51–57, 2014.
- [38] G. Bharath, R. Madhu, S.-M. Chen, V. Veeramani, D. Mangalaraj, and N. Ponpandian, "Solvent-free mechanochemical synthesis of graphene oxide and Fe<sub>3</sub>O<sub>4</sub>-reduced graphene oxide nanocomposites for sensitive detection of nitrite," *Journal of Materials Chemistry A*, vol. 3, no. 30, pp. 15529–15539, 2015.
- [39] I. V. Chernyshova, M. F. Hochella Jr., and A. S. Madden, "Size-dependent structural transformations of hematite nanoparticles. 1. Phase transition," *Physical Chemistry Chemical Physics*, vol. 9, no. 14, pp. 1736–1750, 2007.
- [40] Y. Wang, A. Muramatsu, and T. Sugimoto, "FTIR analysis of well-defined  $\alpha$ -Fe<sub>2</sub>O<sub>3</sub> particles," *Colloids and Surfaces A: Physicochemical and Engineering Aspects*, vol. 134, no. 3, pp. 281–297, 1998.
- [41] C. Tamuly, I. Saikia, M. Hazarika, and M. R. Das, "Reduction of aromatic nitro compounds catalyzed by biogenic CuO nanoparticles," *RSC Advances*, vol. 4, no. 95, pp. 53229–53236, 2014.
- [42] P. Karthik, T. R. Naveen Kumar, and B. Neppolian, "Redox couple mediated charge carrier separation in g-C<sub>3</sub>N<sub>4</sub>/CuO photocatalyst for enhanced photocatalytic H<sub>2</sub> production," *International Journal of Hydrogen Energy*, vol. 45, no. 13, pp. 7541–7551, 2020.
- [43] H. Siddiqui, M. R. Parra, P. Pandey, M. S. Qureshi, and F. Z. Haque, "Performance evaluation of optimized leaf-shaped two-dimension (2D) potassium doped CuO nanostructures with enhanced structural, optical and electronic properties," *Ceramics International*, vol. 46, no. 12, pp. 20404–20414, 2020.
- [44] K. Zhao, C. Ye, X.-B. Chang et al., "Importation and recombination are responsible for the latest emergence of highly pathogenic porcine reproductive and respiratory syndrome virus in China," *Journal of Virology*, vol. 89, no. 20, pp. 10712–10716, 2015.
- [45] S. Ye, M. Yan, X. Tan et al., "Facile assembled biochar-based nanocomposite with improved graphitization for efficient photocatalytic activity driven by visible light," *Applied Catalysis B: Environmental*, vol. 250, pp. 78–88, 2019.
- [46] N. K. Divya and P. P. Pradyumnan, "Photoluminescence quenching and photocatalytic enhancement of Pr-doped ZnO nanocrystals," *Bulletin of Materials Science*, vol. 40, pp. 1405–1413, 2017.
- [47] P. Panchal, D. R. Paul, A. Sharma, P. Choudhary, P. Meena, and S. P. Nehra, "Biogenic mediated Ag/ZnO nanocomposites for photocatalytic and antibacterial activities towards disinfection of water," *Journal of Colloid and Interface Science*, vol. 563, pp. 370–380, 2020.
- [48] C. Parvathiraja and S. Shailajha, "Bioproduction of CuO and Ag/CuO heterogeneous photocatalysis-photocatalytic dye degradation and biological activities," *Applied Nanoscience*, vol. 11, pp. 1411–1425, 2021.
- [49] V. Ramasamy, V. Mohana, and G. Suresh, "Study of Ni:CeO<sub>2</sub> nanoparticles for efficient photodegradation of methylene blue by sun light irradiation," *Indian Journal of Physics*, vol. 92, pp. 1601–1612, 2018.
- [50] H. Guo, C.-G. Niu, D.-W. Huang et al., "Integrating the plasmonic effect and p-n heterojunction into a novel Ag/Ag<sub>2</sub>O/PbBiO<sub>2</sub>Br photocatalyst: broadened light absorption and accelerated charge separation co-mediated highly efficient visible/NIR light photocatalysis," *Chemical Engineering Journal*, vol. 360, pp. 349–363, 2019.
- [51] J. Joo, Y. Ye, D. Kim, J. Lee, and S. Jeon, "Magnetically recoverable hybrid TiO<sub>2</sub> nanocrystal clusters with enhanced photocatalytic activity," *Materials Letters*, vol. 93, pp. 141–144, 2013.
- [52] P. Rai, S.-H. Jeon, C.-H. Lee, J.-H. Lee, and Y.-T. Yu, "Functionalization of ZnO nanorods by CuO nanospikes for gas sensor applications," *RSC Advances*, vol. 4, no. 45, pp. 23604–23609, 2014.
- [53] R. G. Wilson, "Vacuum thermionic work functions of polycrystalline Be, Ti, Cr, Fe, Ni, Cu, Pt, and type 304 stainless steel," *Journal of Applied Physics*, vol. 37, no. 6, pp. 2261–2267, 1966.